Optics Letters

Correlation gating quantifies the optical properties of dynamic media in transmission

DAWID BORYCKI,[1,2] OYBEK KHOLIQOV,[1] AND VIVEK J. SRINIVASAN[1,3,*]

[1]Department of Biomedical Engineering, University of California-Davis, Davis, California 95616, USA
[2]Institute of Physical Chemistry, Polish Academy of Sciences, Kasprzaka 44/52, 01-224 Warsaw, Poland
[3]Department of Ophthalmology and Vision Science, University of California-Davis, Davis School of Medicine, Sacramento, California 96817, USA
*Corresponding author: vjsriniv@ucdavis.edu

Quantifying light transport in turbid media is a long-standing challenge. This challenge arises from the difficulty in experimentally separating unscattered, ballistic light from forward scattered light. Correlation gating is a new approach that numerically separates light paths based on statistical dynamics of the optical field. Here we apply correlation gating with interferometric near-infrared spectroscopy (iNIRS) to separate and independently quantify ballistic and scattered light transmitted through thick samples. First, we present evidence that correlation gating improves the isolation of ballistic light in a thick, intrinsically dynamic medium with Brownian motion. Then, from a single set of iNIRS transmission measurements, we determine the ballistic attenuation coefficient and group refractive index from the time-of-flight (TOF) resolved static intensity, and we determine the reduced scattering and absorption coefficients from the diffusive part of the TOF resolved dynamic intensity. Finally, we show that correlation gating is applicable in intrinsically static media in which motion is induced externally. Thus, for the first time, to the best of our knowledge, the key optical properties of a turbid medium can be derived from a single set of transmission measurements. © 2018 Optical Society of America
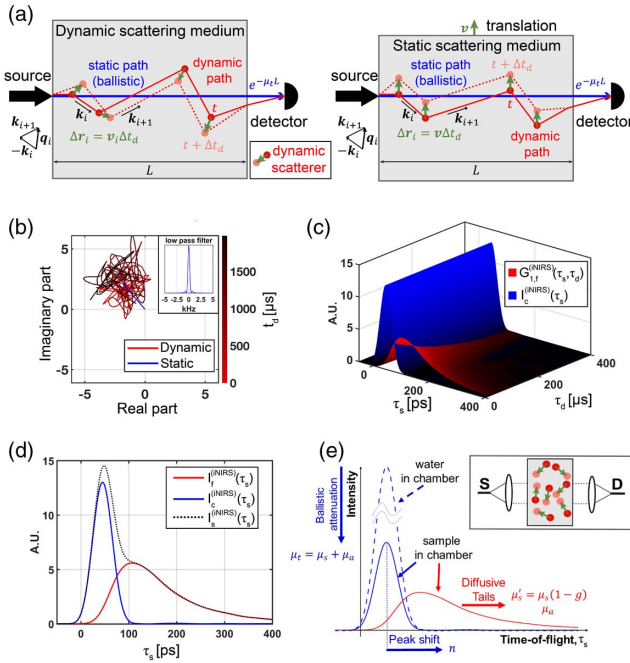
Ballistic light propagation in turbid media is characterized by the absorption coefficient (μ_a) and scattering coefficient (μ_s). In highly scattering media, measuring the ballistic attenuation coefficient, $\mu_t = \mu_s + \mu_a$, poses an experimental challenge. Classically, one performs a collimated transmittance measurement (T_c) on a very thin tissue slice [1]. The attenuation coefficient is then given by $\mu_t = -\log(T_c)/L$, where L is the sample thickness. If μ_a and the reduced scattering coefficient (μ_s') of the tissue are measured with a double integrating sphere [2], then the scattering coefficient and anisotropy can be determined as $\mu_s = \mu_t - \mu_a$ and $g = 1 - \mu_s'/\mu_s$, respectively. In order to accurately measure μ_t (and hence, μ_s), the detection of scattered light in collimated transmittance must be avoided. This is challenging, particularly in biological tissues that are

highly forward scattering, and the angular or spatial rejection of scattered light is difficult. A rough guideline for collimated transmittance is that the sample thickness should be on the order of a scattering mean free path or less ($L \lesssim 1/\mu_s$) [1]. A more precise criterion for rejecting scattered light depends on the relationship between the scattering phase function, $p(\theta)$, and the detector acceptance angle [3]. Thin samples are preferred, because the detection of any scattered light will underestimate μ_t and μ_s. However, thin samples are difficult to prepare and prone to desiccation [1]. Another approach, based on reflectance confocal microscopy and Monte Carlo modeling, achieves simultaneous measurements of scattering anisotropy $g = \cos(\theta)$ and μ_s in non-absorbing media, but requires assumptions about the form of $p(\theta)$ [4].

Here we address the challenge of determining μ_s in transmission. Our approach separates ballistic light from forward scattered transmitted light in samples thicker than $1/\mu_s$. First, we use interferometric near-infrared spectroscopy (iNIRS) to achieve time-of-flight (TOF) resolved measurements of the optical field [5]. Secondly, we argue that field dynamics are a sensitive indicator of the presence of momentum transfer. In particular, the scattered light field fluctuates due to sample dynamics, even for small deflection angles, whereas the ballistic light field does not fluctuate. Hence, the ballistic intensity is the modulus-squared of the constant (or static) field that does not decorrelate, while the scattered intensity is the modulus-squared of the dynamic (or fluctuating) field that decorrelates over time. Based on these insights, we apply an approach called *correlation gating*, which independently quantifies dynamic and static intensity [6], to assess scattered and unscattered light, respectively, in transmission. We use the diffusive part of the dynamic (scattered) intensity to determine μ_s' and μ_a [6]. For the first time, to the best of our knowledge, we analyze the attenuation and peak shift of the static (ballistic) intensity to quantify μ_t and group refractive index, n. Our results show that correlation gating represents a novel approach for separating light paths in turbid media, analogous to TOF gating [7,8], polarization gating [9,10], and spatial gating [11]. Correlation gating can cooperate with other gating methods to improve ballistic light measurements in thick media.

The approach of quantifying optical properties in transmission with correlation gating is shown in Fig. 1(a). In this Letter, the method is applied to the iNIRS complex-valued mutual coherence function, $\Gamma_{rs}(\tau_s, t_d)$, henceforth referred to as the "field," [5] where τ_s is the TOF, and t_d is the delay time. For a sample with intrinsic Brownian motion, the dynamic field (red) fluctuates in t_d around the constant (or static) field (blue) [Fig. 1(b)], obtained here by applying a low-pass filter (inset) in t_d. Scattered paths, which experience phase shifts ($\Delta r_i \cdot q_i$) due to scatterer displacement (Δr_i) and momentum transfer (q_i) at each scattering event [Fig. 1(a)], are responsible for the dynamic field. It is reasonable to assume that unscattered paths are responsible for the static field component: this assumption will be further examined below. The field autocorrelation is estimated as $G_1^{(iNIRS)}(\tau_s, \tau_d) = \langle \Gamma_{rs}^*(\tau_s, t_d) \Gamma_{rs}(\tau_s, t_d + \tau_d) \rangle_{t_d}$, where τ_d is the time lag. The measured $G_1^{(iNIRS)}$ represents the true autocorrelation, G_1, convolved in τ_s with the instrument response function (IRF), $I_0(\tau_s)$ [5]. As $\tau_d \to \infty$, $G_1^{(iNIRS)}(\tau_s, \tau_d)$


Fig. 1. Correlation gating, a new method to independently assess ballistic and diffusive light transport in turbid media, is founded on the physical principle that optical field dynamics can distinguish scattered from ballistic light in transmission. (a) Method applies to media with intrinsic dynamics (left) or dynamics induced externally (right). (b) For IL-20% diluted in water ($c_p \approx 4.8\%$), a suspension with intrinsic Brownian motion, light paths with momentum transfer (q) experience random phase shifts and decorrelate. Hence, the field of ballistic light is constant (static) and separable by a low-pass filter (inset), whereas the field of scattered light fluctuates in time. (c)-(d) Static (ballistic) and dynamic (scattered) light paths can be separated and independently quantified via the field autocorrelation function. (e) Ballistic attenuation (μ_t), ballistic peak shift, and diffusive tails together determine the group refractive index (n), absorption (μ_a), reduced scattering (μ_s'), scattering (μ_s), and scattering anisotropy (g). Thus, the optical properties can be quantified from a single measurement set obtained by a single modality. (a) Sketch of the experiment, (b) field components ($\tau_s = 45$ ps), (c) un-normalized field autocorrelation, (d) TPSFs, and (e) determination of the optical properties.

decays to the TOF-dependent constant intensity $I_c^{(iNIRS)}(\tau_s)$ instead of zero. Accordingly, the autocorrelation contains two terms [Fig. 1(c)]: $G_1^{(iNIRS)}(\tau_s, \tau_d) = I_c^{(iNIRS)}(\tau_s) + G_{1,f}^{(iNIRS)}(\tau_s, \tau_d)$, where $G_{1,f}^{(iNIRS)}(\tau_s, \tau_d)$ is the fluctuating (dynamic) field autocorrelation, whose decay rate depends on the statistics of the phase shifts along different paths [12]. Thus, the sample (total) $[I_s^{(iNIRS)}(\tau_s) = G_1^{(iNIRS)}(\tau_s, 0)]$, constant (static) $[I_c^{(iNIRS)}(\tau_s) = G_1^{(iNIRS)}(\tau_s, \tau_d \to \infty)]$, and fluctuating (dynamic) $[I_f^{(iNIRS)}(\tau_s) = I_s^{(iNIRS)}(\tau_s) - I_c^{(iNIRS)}(\tau_s)]$ temporal point spread functions (TPSFs) can be determined [Fig. 1(d)], and used to quantify the optical properties [Fig. 1(e)]. First, the attenuation of the static TPSF determines the ballistic attenuation coefficient (μ_t). Secondly, the mean arrival time or TOF centroid of the static TPSF, $\bar{\tau}_{s,c} = \int \tau_s I_c^{(iNIRS)}(\tau_s) d\tau_s / \int I_c^{(iNIRS)}(\tau_s) d\tau_s$, determines the sample group index, $n = c \bar{\tau}_{s,c} / L$, where c is the speed of light (in practice, limits of integration are the TOF range where the static TPSF exceeds the noise floor). Thirdly, the reduced scattering coefficient (μ_s') and absorption coefficient (μ_a) are determined by fitting the dynamic TPSF to the solution of the diffusion equation for a homogeneous, turbid, rectangular parallelepiped of width l_x, height l_y, and thickness l_z along the propagation direction. The TOF-resolved transmittance is given by Eqs. (7) and (8) from Ref. [13] with the detector positioned at $(x = l_x/2, y = l_y/2, z = l_z)$. Fourthly, the resulting μ_a is subtracted from μ_t to obtain μ_s. Lastly, given μ_s and μ_s', the scattering anisotropy is determined as $g = 1 - \mu_s'/\mu_s$.

To experimentally validate our approach, we filled a parallelepiped glass cuvette ($l_x = l_z = 10$ mm, $l_y = 30$ mm) with 3 mL of deionized water. Then, increasing volumes (125–220 μL in steps of 5 μL) of Intralipid-20% (IL-20%) were added to the cuvette and mixed *in situ* to achieve IL-20% concentrations of 4.00%–6.83%. We neglected the slight increase in l_y as IL-20% was added. The collimated light beam from an 855 nm rapidly tuned laser illuminated the sample and the transmitted light was combined with light travelling a reference path with matched polarization (not shown). Note that the finite mode field area and acceptance cone of the single-mode fiber used for detection help to reject scattered light. The interference spectrum was measured repeatedly over time using a setup modified from Ref. [5] (TOF resolution ~45 ps FWHM, static coherence length > 100 m). For each sample, a dataset composed of 40,000 iNIRS signals (80,000 total forward and backward sweeps) was acquired at a tuning speed of 50 kHz (100 kHz sweep rate). Lastly, the reference arm signal alone was recorded to estimate the background. Each dataset was processed to yield $\Gamma_{rs}(\tau_s, t_d)$ [14], which were autocorrelated and background-corrected to estimate static and dynamic TPSFs [5].

Static TPSFs with varying IL-20% concentrations (c_p) are shown in Fig. 2. As predicted by the Beer–Lambert law for ballistic attenuation, the static TPSF attenuation on a logarithmic scale is linear in c_p [Fig. 2(a)]. In addition, the static TPSF shape is identical to the water TPSF, or IRF, until $c_p < 5.5\%$ [Fig. 2(b)]. This is consistent with a delta function TOF distribution for static photons. We also see that for $c_p < 5.5\%$, both the peak location $\tau_{s,peak}$ and centroid $\bar{\tau}_{s,c}$ are slightly larger than the ballistic TOF through the water sample (~44.3 ps for cuvette thickness of 10 mm) [Figs. 2(a)–2(c)]. Using centroids for $c_p \leq 5.5\%$, we get a group index of $n = 1.33 \pm 0.03$. This
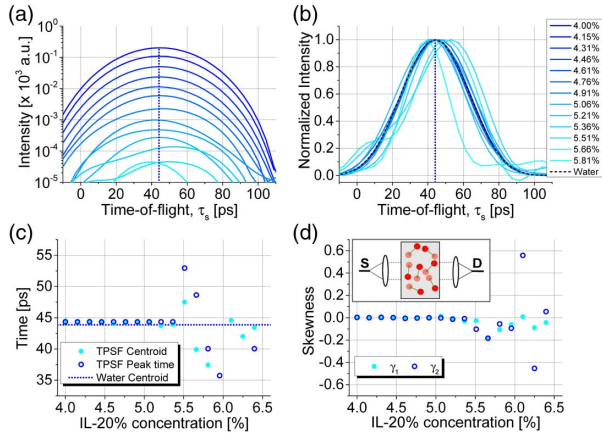
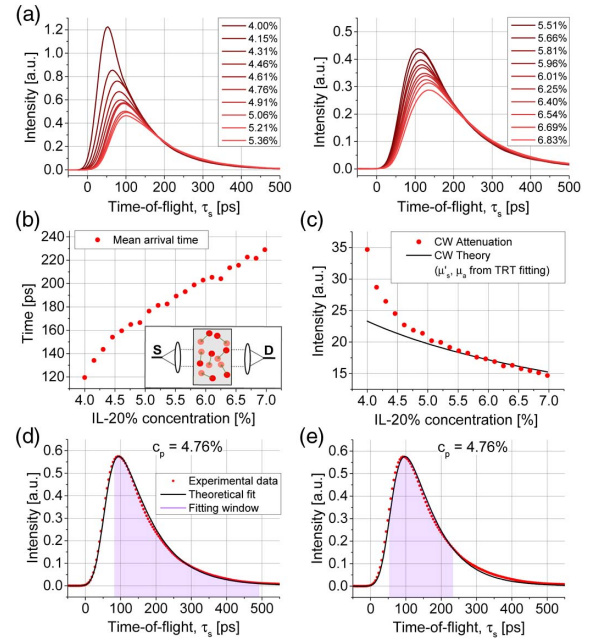**Fig. 2.** Static TPSFs for various IL-20% concentrations (c_p). As c_p increases, the TPSFs are attenuated (a), but their shapes, after normalization, are unchanged (b). The mean arrival time, peak time (c), and TPSF skewness (d) are similar to the water TPSF. For larger concentrations, noise begins to affect measurements. Together, these results support the assertion that the static component represents ballistic light.

range is reasonable for water ($n = 1.329$ [15]) with 4%–7% added IL-20% [16].

Lastly, skewness was estimated by two measures: γ_1, which is the third standardized moment of the static TPSF, and $\gamma_2 = (\bar{\tau}_{s,c} - \tau_{s,\text{peak}})/\sigma$, where σ is the standard deviation of $I_c^{(\text{iNIRS})}$. Static TPSF skewness [Fig. 2(d)] is small until $c_p < 5.5\%$. If the static TPSF included scattered light, the peak time, TOF centroid, and skewness would systematically increase for larger concentrations. The observed random changes in static TPSF shape at higher concentrations in Fig. 2 are therefore most likely attributable to a degradation in signal-to-noise ratio. Taken together, the data in Fig. 2 support our assertion that the static intensity represents ballistic light. We also anecdotally observed that if the detector was misaligned, static intensity decreased more rapidly than dynamic intensity, further supporting this conclusion.

Dynamic TPSFs are attenuated, broadened, and delayed with increasing c_p [Fig. 3(a)]. The mean arrival time, $\bar{\tau}_{s,f}$, of the dynamic TPSF increases rapidly for $c_p < 4.7\%$, and more slowly for $c_p > 4.7\%$ [Fig. 3(b)]. Similarly, the attenuation of TOF-integrated dynamic, or fluctuating, TPSFs, $\mathcal{I}_f^{(\text{iNIRS})} = \int I_f^{(\text{iNIRS})}(\tau_s)\mathrm{d}\tau_s$, is rapid for $c_p < 4.7\%$, and less rapid for $c_p > 4.7\%$ [Fig. 3(c)]. These observations, together with the dynamic TPSF shapes, suggest that for low c_p, the early TOF portion of the dynamic TPSF includes non-diffuse paths.

The late TOF tails, which reach a similar asymptotic decay independent of c_p, are more likely to be diffuse. Since the diffusion approximation may not be valid for the early TOF part of the dynamic TPSF, we define a concentration (c_p)-dependent fitting window (FW), which starts at $\tau_s^{(\text{FW})}(c_p) = \frac{n\ell}{c\mu_s'(c_p)} + \delta\tau_s$, where $\delta\tau_s$ accounts for the finite TOF resolution (IRF width). Since the asymptotic TPSF slope encodes μ_a, whereas the TPSF peak encodes μ_s', we fix $\delta\tau_s = 50$ ps, and choose the parameter ℓ, depending on the fitting mode. When fitting for absorption, $\ell = 6$, so FW is focused on the asymptotic TPSF slope; when fitting for reduced scattering, $\ell = 0$, and FW covers the TPSF


Fig. 3. Dynamic TPSFs for various IL-20% concentrations (c_p). (a) In contrast to the static TPSFs (Fig. 2), dynamic TPSFs are broadened and delayed as c_p increases. (b) Thus, the mean dynamic TPSF arrival time increases with c_p. (c) For $c_p > 4.7\%$, the TOF-integrated dynamic intensity decreases with c_p, but less rapidly than the static TPSFs, and in agreement with the CW diffusion theory [Eqs. (13) and (14) from Ref. [13]] (black line). (d) and (e) Representative fits of dynamic TPSF to diffusion theory for the tail- and peak-focused FWs, used for absorption and scattering, respectively.

peak. To determine $\tau_s^{(\text{FW})}(c_p)$, we assume an approximate value of $\mu_s' = 17$ mm^{-1} for IL-20% at 855 nm [17]. Thus, increasing c_p shifts the FW start to earlier TOFs. The FW continues until the TPSF tail is above the threshold of 0.01 [absorption FW Fig. 3(d)] or 0.175 [reduced scattering FW, Fig. 3(e)]. The diffuse portion of the dynamic TPSF is then fit via nonlinear regression by $T(\tau_s) * I_0(\tau_s)$ over the FW [shaded region in Figs. 3(d) and 3(e)], where $*$ is the convolution in τ_s [14]. The reduced scattering and absorption coefficients for varying IL-20% concentrations are shown in Figs. 4(a) and 4(b). An average absorption of $\mu_a = (4.31 \pm 0.32) \times 10^{-3}$ mm^{-1}, close to that of water, was obtained, and the reduced scattering coefficients were fit by a line with zero intercept, leading to μ_s' of 17.1 ± 0.1 mm^{-1} for pure IL-20%. The value of μ_s' is slightly smaller than that obtained with a double-integrating sphere ($\mu_s' \approx 19$ mm^{-1}) [18].

The TOF-integrated static or constant [$\mathcal{I}_c^{(\text{iNIRS})}$] and total sample [$\mathcal{I}_s^{(\text{iNIRS})}$] TPSFs are plotted as a function of c_p in Fig. 4(c). $\mathcal{I}_s^{(\text{iNIRS})}$, corresponding to conventional collimated transmittance, includes both ballistic and scattered components, each of which is attenuated at a different rate. For $c_p < 4.7\%$, ballistic light dominates $\mathcal{I}_s^{(\text{iNIRS})}$, so $\mathcal{I}_c^{(\text{iNIRS})}$ (cyan circles) and $\mathcal{I}_s^{(\text{iNIRS})}$ (black squares) are comparable. For $c_p > 5\%$ scattered light [$\mathcal{I}_f^{(\text{iNIRS})} = \mathcal{I}_s^{(\text{iNIRS})} - \mathcal{I}_c^{(\text{iNIRS})}$] dominates (red diamonds).

Thus, as shown in Fig. 4(c), $\mathcal{I}_s^{(\text{iNIRS})}$ underestimates the attenuation coefficient ($\mu_t = 25.4$ mm^{-1}) compared with $\mathcal{I}_c^{(\text{iNIRS})}$ ($\mu_t = 45.1$ mm^{-1}).
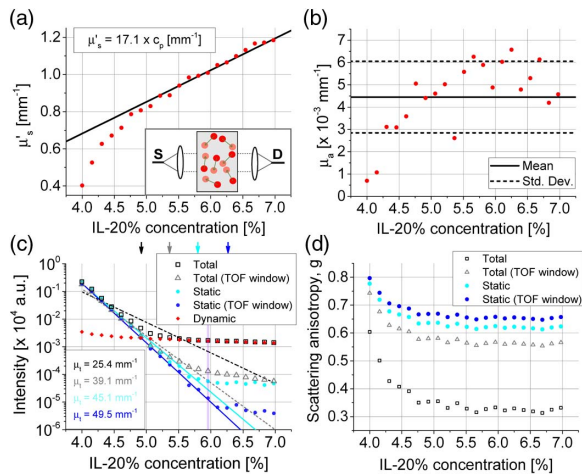
Fig. 4. Correlation gating enables the independent analysis of ballistic (Fig. 2) and diffusive (Fig. 3) light transport from a single measurement set. Diffuse optical properties (μ_a, μ_s') are determined from diffusive transport (a) and (b), and the attenuation coefficient ($\mu_t = \mu_s + \mu_a$) is determined from ballistic transport (c). The lines represent fits over $4.0 \leq c_p \leq 5.9\%$ (vertical line) for total (black and gray dashed) and static (cyan and blue solid) components. The arrows in the top margin indicate the c_p values at which data start to depart from ballistic attenuation. μ_s' and $\mu_s = \mu_t - \mu_a$ together yield $g = 1 - \mu_s'/\mu_s$ (d). Importantly, in a standard collimated transmittance measurement without correlation gating (black squares and gray triangles), μ_t and g are underestimated, due to the inadequate rejection of scattered light.

To explore the synergy between correlation gating and time gating, the integration window was set to 25–75 ps to encompass the ballistic TOF. The resulting TOF-windowed static (blue circles) and total (gray triangles) TPSF intensities are shown in Fig. 4(c). The colored arrows in the upper margin mark the concentration at which departure from the Beer–Lambert law is first observed. Time gating alone (gray triangles) improves the ability to distinguish ballistic from scattered light, but not as well as correlation gating alone (cyan circles). Importantly, both gating methods cooperate to extend the range over which the ballistic attenuation is observed to $c_p \sim 6.1\%$ (blue circles). This concentration corresponds to ~30 scattering lengths. Applying both gating methods together yields an estimate of $\mu_t = 49.5$ mm^{-1} (blue line). A published work, which relied on the angular rejection of scattered light alone, reported $\mu_t = 47.6$ mm^{-1} [18]. Assuming that water dominates absorption for all c_p of interest, the average μ_a value is then subtracted from μ_t to determine corresponding scattering coefficients and anisotropies [Fig. 4(d)]. The scattering anisotropy, similar to the attenuation coefficient, is underestimated if correlation gating is not used. Thus, correlation gating improves the separation of ballistic from scattered light.

Finally, we applied correlation gating to intrinsically static gelatinized samples with variable IL-20% content (3.5%–7.0% in steps of 0.5%). Each sample was translated perpendicular to the beam direction over 5 mm with velocity, $v = 0$ mm/s or 10 mm/s. Each dataset was processed to determine total sample, constant (static), and fluctuating (dynamic) TPSFs. Sample translation [Fig. 1(a)] and gel oscillations (caused by acceleration) induce dynamics and impart phase shifts to scattered
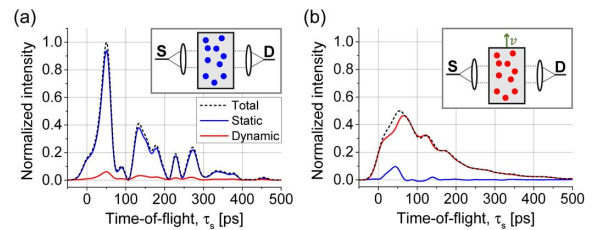
Fig. 5. Total, static, and dynamic TPSFs for gel with 4.5% IL-20% content at (a) $v = 0$ mm/s and (b) $v = 10$ mm/s. All TPSFs were normalized to the peak value of the total component for $v = 0$ mm/s. (a) Static sample and (b) static sample with induced dynamics.

light. Thus, the static component recovers ballistic light for $v = 10$ mm/s [Fig. 5(b)], but not for $v = 0$ mm/s [Fig. 5(a)].

Assuming $n = 1.33$, the dynamic TPSF was fit by $T(\tau_s) * I_0(\tau_s)$ to determine $\mu_s' = 17.2 \pm 0.3$ mm^{-1} and $\mu_a = (4.7 \pm 0.9) \times 10^{-3}$ mm^{-1}.

Building on the physical insight that field dynamics can separate scattered and ballistic light in transmission, this Letter introduces correlation gating to comprehensively quantify the optical properties of turbid media. The approach is based on the physical principle that for transmission through a uniformly dynamic medium, where all scattering events with momentum transfer cause phase shifts, the dynamic intensity corresponds to scattered light, and the static intensity corresponds to ballistic light. While we have demonstrated its application to iNIRS, correlation gating also could be applied to optical coherence tomography or any method that provides access to the optical field.

REFERENCES

1. S. L. Jacques, Phys. Med. Biol. **58**, R37 (2013).
2. J. W. Pickering, S. A. Prahl, N. van Wieringen, J. F. Beek, H. J. Sterenborg, and M. J. van Gemert, Appl. Opt. **32**, 399 (1993).
3. L. V. Wang and H. Wu, *Biomedical Optics: Principles and Imaging* (Wiley, 2012).
4. R. V. Samatham, S. L. Jacques, and P. J. Campagnola, J. Biomed. Opt. **13**, 041309 (2008).
5. D. Borycki, O. Kholiqov, and V. J. Srinivasan, Optica **3**, 1471 (2016).
6. D. Borycki, O. Kholiqov, and V. J. Srinivasan, Opt. Lett. **42**, 591 (2017).
7. L. Wang, P. P. Ho, C. Liu, G. Zhang, and R. R. Alfano, Science **253**, 769 (1991).
8. M. R. Hee, E. A. Swanson, J. A. Izatt, J. M. Jacobson, and J. G. Fujimoto, Opt. Lett. **18**, 950 (1993).
9. H. Horinaka, M. Osawa, K. Hashimoto, K. Wada, and Y. Cho, Opt. Lett. **20**, 1501 (1995).
10. S. L. Jacques, J. R. Roman, and K. Lee, Lasers Surg. Med. **26**, 119 (2000).
11. G. E. Anderson, F. Liu, and R. R. Alfano, Opt. Lett. **19**, 981 (1994).
12. G. Maret and P. E. Wolf, Z. Phys. B **65**, 409 (1987).
13. A. Kienle, J. Opt. Soc. Am. A **22**, 1883 (2005).
14. O. Kholiqov, D. Borycki, and V. J. Srinivasan, Opt. Express **25**, 28567 (2017).
15. G. M. Hale and M. R. Querry, Appl. Opt. **12**, 555 (1973).
16. H. Ding, J. Q. Lu, K. M. Jacobs, and X.-H. Hu, J. Opt. Soc. Am. A **22**, 1151 (2005).
17. R. Michels, F. Foschum, and A. Kienle, Opt. Express **16**, 5907 (2008).
18. B. Aernouts, E. Zamora-Rojas, R. Van Beers, R. Watté, L. Wang, M. Tsuta, J. Lammertyn, and W. Saeys, Opt. Express **21**, 32450 (2013).